Single-Crystal Model of Highly Efficient Water-Splitting Photocatalysts: A KTaO3 Wafer Doped with Calcium Cations

Fujiwara, Tomoya ; Sasahara, Akira ; Happo, Naohisa ; Kimrua, Koji ; Hayashi, Kouichi ; Onishi, Hiroshi

(Citation)
Chemistry of Materials,32(4):1439-1447

(Issue Date)
2020-02-25

(Resource Type)
journal article

(Version)
Version of Record

(URL)
https://hdl.handle.net/20.500.14094/90007787

CHEMISTRY OF MATERIALS

pubs.acs.org/cm

Article

Single-Crystal Model of Highly Efficient Water-Splitting Photocatalysts: A $KTaO_3$ Wafer Doped with Calcium Cations

Tomoya Fujiwara, Akira Sasahara, Naohisa Happo, Koji Kimura, Kouichi Hayashi, and Hiroshi Onishi*

Cite This: *Chem. Mater.* 2020, 32, 1439−1447

Read Online

ACCESS | Metrics & More | Article Recommendations | Supporting Information

ABSTRACT: Alkali tantalates, $NaTaO_3$ and $KTaO_3$, are known as highly efficient semiconductor photocatalysts for the overall water-splitting reaction when properly doped with foreign metal cations. Characterizing surface reaction sites is needed for further development. In this study, (001)-oriented $KTaO_3$ wafers were doped with Ca cations thorough a solid-state reaction to provide platforms for surface science studies. X-ray diffraction showed a Ca-rich perovskite-structured surface layer that covers the Ca-poor or pristine $KTaO_3$ substrate. The lattice of the surface layer was contracted and rotated relative to the substrate lattice. The heteroepitaxial junction of the surface layer on the substrate mimicked the core−shell structure that is found in real photocatalyst particles. Nanometer-scale islands spontaneously appeared on the surface to correct the lattice mismatch across the surface−substrate junction. X-ray fluorescence holography was applied to determine the local, atom-scale structure around Ca cations in the host lattice. Atom distributions reconstructed from Ca Kβ fluorescence holograms suggested that K and Ta cations were simultaneously exchanged with Ca cations. Local lattice deformation was quantitatively deduced around the Ca cations occupying the two different sites. The major features of real photocatalysts—heteroepitaxial surface−bulk junctions, surface restructuring to correct lattice mismatches, and simultaneous cation exchange—were reproduced in the doped wafers. The ability of X-ray fluorescence holography to determine a local structure around doping cations was also demonstrated.

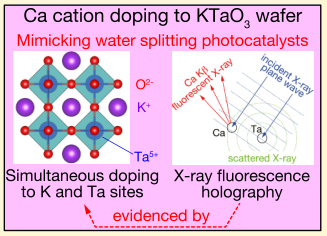

1. INTRODUCTION

Alkali tantalates, $NaTaO_3$ and $KTaO_3$, are highly efficient semiconductor photocatalysts that split pure water to produce hydrogen−oxygen mixed bubbles. The apparent quantum yield, which is defined as the number ratio of electrons (or holes) consumed in the reaction over the number of incident photons, exceeded 50% when $NaTaO_3$ was doped with La cations and modified with a NiO cocatalyst.[1,2] Doping with lanthanoid (Pr, Nd, Sm, Gd, Tb, or Dy)[1] and alkaline earth metal (Ca, Sr, or Ba)[3−5] cations improved water-splitting yield on $NaTaO_3$ comparably. Potassium tantalate ($KTaO_3$) photocatalysts doped or undoped with metal cations also provided good quantum yields for the water-splitting reaction.[6−11] The further application of these photocatalysts was examined in CO_2 reduction,[12−14] CH_4 steam reforming,[15,16] and glucose reforming[17] reactions.

The mechanisms behind the successful cation doping of tantalate photocatalysts have been studied, as recently reviewed by Onishi.[18] The infrared absorption of band gap-excited photocatalysts showed that successful doping reduced the electron−hole recombination rate, and the steady-state population of charge carriers accordingly increased. In-depth studies focused on Sr doping to $NaTaO_3$ revealed that Na and Ta cations in the host lattice were simultaneously doped to produce a $NaTaO_3$−$Sr(Sr_{1/3}Ta_{2/3})O_3$ solid solution. Strontium cations segregated in the solid−solution particles to produce junctions of the Sr-rich surface and Sr-poor bulk. The bottom of the conduction band lifted up at the Sr-rich surface, and excited electrons were driven to the Sr-poor bulk, which left holes at the surface. Thus, electrons and holes were separated in space.

In addition to the hypothesized charge separation, surface reaction centers on the solid−solution photocatalysts should be investigated for further development. A series of centimeter-sized, well-defined photocatalyst crystals doped with metal cations are required to characterize reaction centers. Advanced analytical methods functional in water, for example, scanning probes and nonlinear optical spectroscopy, should be feasible on photocatalysts in the form of centimeter-sized crystals.

The authors examined Ba-containing $NaTaO_3$ films[19] epitaxially grown on $SrTiO_3$(001) wafers to satisfy the requirement. In this study, commercially available, single-crystal $KTaO_3$ wafers were doped with Ca cations to mimic the highly efficient alkali tantalate photocatalysts. Single-crystal $KTaO_3$ wafers were applied to the electrochemical[20,21] and photoelectrochemical[22] oxidation of water.

Potassium tantalate has a perovskite structure with a perfect cubic symmetry and a unit cell length of 0.399 nm,[23] as illustrated in Figure 1. Sodium tantalate has a perovskite structure with a slightly distorted orthorhombic symmetry

Received: October 7, 2019
Revised: January 18, 2020
Published: January 21, 2020

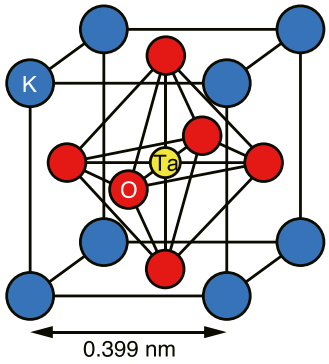

Figure 1. Cubic unit cell of $KTaO_3$.

(*Pbnm*) at room temperature.[24] An orthorhombic cell contains four $NaTaO_3$ units. A cube with 0.389 nm sides, the volume of which corresponds to one-fourth that of the orthorhombic cell volume, is effectively assigned to a unit cell in the pseudo cubic lattice. Hence, $KTaO_3$ is analogous to $NaTaO_3$ with a lattice expansion of 2.5%.

Metal cation doping is frequently performed to control electric, magnetic, or optical properties of single-crystal metal oxides. However, the applications for photocatalyst modeling are limited. Rhodium,[25] iridium,[26] and niobium[27] doping was exploited to control the charge carrier density in $SrTiO_3$ films. Rutile TiO_2(110) wafers were doped solely[28,29] or simultaneously[30] with Cr and Sb cations to examine visible-light sensitized TiO_2 photocatalyst models using scanning probe microscopy.

The present study is focused on a semiconductor with a band gap of 3.6 eV.[31] To sensitize the wide-band gap semiconductor to visible light, double cation doping[32−40] has been examined for creating mid-gap electronic states. Oxynitride formation by nitrogen anion doping is achieved as well.[41−47] The methods, results, and interpretations accumulated in this study are to be applied to many other materials including visible-light sensitized tantalates.

2. EXPERIMENTAL SECTION

2.1. Materials. A one-side polished, (001)-oriented $KTaO_3$ wafer with dimensions of 10 × 10 × 0.5 mm^3 (crystal base) was used as the substrate. Calcium carbonate (Wako, 99.5%) was suspended in water with a concentration of 0.1 mol l^{-1}. A droplet of the suspension with a volume of 0.2 mL was placed on the wafer and dried. The dried wafer was calcined in air at 1173 K for 6 h and then at 1273 K for 12 h. The calcined wafer was washed with an aqueous HCl solution (10 wt %) for 10 min at RT to remove Ca-containing compounds that were left on the wafer surface, if any. These procedures followed the solid-state preparation of $NaTaO_3$ photocatalyst particles doped with Sr cations that are used for the X-ray absorption characterization.[48]

The composition of the washed wafer was determined to have a molar ratio of Ca/K/Ta = 22:30:48 by detecting Ca Kα, K Kα, and Ta Lα fluorescence X-rays with a laboratory-scale spectrometer (Shimadzu, EDX-720). Another wafer without doping had a ratio of K/Ta = 51:49. Doping with Ca cations reduced the concentration of K cations rather than that of Ta cations. However, a simple substitution of K cations by Ca cations cannot be confirmed because the escape depth of the three fluorescent X-rays are not the same. The escape depth of Ca Kα, K Kα, and Ta Lα emissions was estimated in $KTaO_3$ to be 1.9, 1.4, and 11.8 μm, respectively. The penetration depth of Ca cations into the wafer is unknown and is possibly smaller than the escape depths.

2.2. Characterization. The crystallographic phase was determined using an X-ray diffractometer (Rigaku, SmartLab) with a Cu Kα source at Hyogo Prefectural Institute of Technology. To determine the short-range ordered structure around Ca cations embedded in the $KTaO_3$ host lattice, X-ray fluorescence holograms of Ca Kβ and Ta Lα fluorescent X-rays were observed by using the beam line 13XU at the SPring-8 synchrotron facility. Curved graphite crystals[49] were used to focus the fluorescent X-ray on a solid-state detector. The obtained holograms were processed with a 3D-AIR-IMAGE code,[50] in which the short-range ordered structure around a fluorescing element, Ca or Ta, was reconstructed using Barton's multiple energy algorithm.[51] The doped wafer was finally coated with osmium and observed with a scanning electron microscope (Hitachi High-Technologies, S-4800) at Kanagawa Institute of Industrial Science and Technology to examine the nanometer-scale topography of the surface.

3. RESULTS AND DISCUSSION

3.1. Crystallographic Phase. The crystallographic phase and orientation of the doped wafer were checked by X-ray diffraction. Figure 2 shows the observed diffraction patterns with a definition of measurement angles in the inset of panel (a). With χ = 0° and ϕ = 0°, four peaks appeared at 2θ = 22, 45, 71, and 101°, which were assigned to (00n) diffractions of $KTaO_3$ with n = 1−4, respectively. The presence of (00n) peaks together with the absence of other diffraction peaks indicated that (001) planes were stacked parallel to the wafer surface with a plane distance of 0.40 nm. The surface layer of the wafer, the thickness of which is given by the penetration depth of Cu Kα X-ray, remained (001)-oriented $KTaO_3$ even doped with Ca cations.

Diffraction patterns were further observed at χ = 45° to obtain additional surface-sensitive information. At ϕ = 0°, a sharp peak was present at 2θ = 31.6° that was assigned to the (011) diffraction of the bulk $KTaO_3$ with a lattice constant of 0.400 nm. By rotating the wafer to have a finite ϕ, −0.9 or +1.0°, a diffraction peak at 2θ = 33.0° appeared, as shown in Figure 2b. Because the contribution of bulk $KTaO_3$ is reduced by the finite ϕ deviations from the Bragg−Brentano condition, the diffraction in a thin surface layer affected by doping was recognized. By assuming that the thin surface layer is epitaxial to the bulk $KTaO_3$, the (011) diffraction at 33.0° predicted a lattice constant of 0.383 nm with a contraction of 4% relative to that of the bulk $KTaO_3$. The possible reason for the lattice contraction will be described in 3.3.

The epitaxial relation in in-plane directions was checked and confirmed in Figure 2c by scanning ϕ from −45 to +315° at χ = 45°. The diffraction pattern obtained with 2θ = 31.6° exhibited four peaks at 0, 90, 180, and 270°, which represent the four-fold symmetry of the bulk $KTaO_3$. Another ϕ scan with 2θ = 33.0° presented an identical, four-fold diffraction pattern to confirm the epitaxial relation of the surface layer affected by doping, which should be rich in Ca concentration, on the $KTaO_3$ substrate. However, the distance of neighboring (011) planes decreased by 4% in the surface layer, as described in the preceding paragraph. A mismatch should be present across the boundary of the surface layer and bulk substrate. The surface layer may rotate on the substrate to reduce strain energy. This was the case here. Two ϕ scans with 2θ = 31.6 and 33.0° were conducted around ϕ = 0° and are shown in Figure 2d. Diffraction with 2θ = 31.6°, which represented the in-plane orientation of the $KTaO_3$ substrate, exhibited one sharp peak at 0°. With 2θ = 33.0°, where the contribution of the surface layer was dominant, two broad peaks appeared at ±1.0° with equal intensities. The Ca-rich surface layer

https://dx.doi.org/10.1021/acs.chemmater.9b04094
Chem. Mater. 2020, 32, 1439−1447

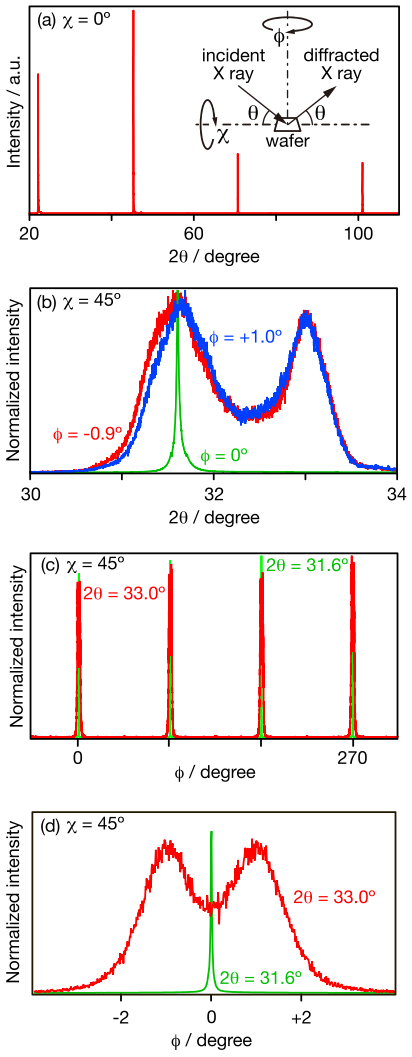

Figure 2. X-ray diffraction patterns of the $KTaO_3$ wafer doped with Ca cations. (a) Diffraction observed in a 2θ scan with $\chi = 0°$ and $\phi = 0°$. The definition of the angles is illustrated in the inset. The wafer surface was perpendicular to the ϕ axis when $\chi = 0°$. (b) Diffraction patterns observed in 2θ scans with $\chi = 45°$. ϕ was set to 0 (green curve), −0.9 (red curve), and +1.0° (blue curve). (c) Diffraction observed in ϕ scans with $\chi = 45°$. 2θ was set to 31.6 (green curve) and 33.0° (red curve). (d) Diffraction observed in ϕ scans around $\phi = 0°$ with $\chi = 45°$. 2θ was set to 31.6 (green curve) and 33.0° (red curve). $\phi = 0°$ is defined to be at the peak of the green curve. The intensity was normalized to the most intense peak in each diffraction pattern.

provided crystalline domains rotated by ±1.0° when covering the bulk lattice.

An and Onishi determined that $NaTaO_3$ photocatalysts doped with Sr cations through a solid-state reaction[52] or crystallization in NaCl flux[53] are composed of a $NaTaO_3$–$Sr(Sr_{1/3}Ta_{2/3})O_3$ solid solution. They further proposed[52] core–shell structured particles with Sr-rich shells covering Sr-poor cores and evidenced[53] with element mapping by scanning transmission electron microscopy. The two phases described here, the $KTaO_3$ substrate and the Ca-containing surface layer covering the substrate in a heteroepitaxial manner, mimicked the core–shell structured $NaTaO_3$ photocatalysts. Calcium-cation incorporation can occur in our $KTaO_3$ substrate as well as the surface layer, though we found no sign of lattice contraction or expansion in the substrate. Diffraction peaks are not sensitive to a small amount of incorporated Ca cations.

3.2. Nanometer-Scale Topography. The lattice mismatch with the rotational displacements across the boundary of the two phases can modify the nanometer-scale topography of the Ca-containing surface layer. A crystalline domain of the surface layer rotated clockwise by 1° on the $KTaO_3$ substrate is illustrated in Figure 3a. The black-colored meshes represent the substrate lattice. The shrunken and rotated lattice of the surface layer is shown with red-colored meshes. The two square meshes interfere to produce a moiré, which is recognized as bright squares rotated clockwise by 24° relative to the substrate lattice. The side length of the moiré lattice is 8.6 nm. The degree of mismatch is periodically modulated according to the moiré. The two crystalline lattices are out-of-phase at the center of the bright squares and in-phase at the corner of the squares. We assume that the periodically modulated mismatch generates steps running parallel to the sides of the moiré lattice on the wafer surface, thereby correcting the mismatch at the boundary of the surface layer and substrate. To verify the assumption, scanning electron micrographs of the doped wafer were compared with the moiré lattice. A typical micrograph is shown in Figure 3b where step edges are enhanced by differentiating the raw image. Round-square shaped islands of 50–100 nm side length appeared. The edges of the islands were not parallel to the [100] or [010] directions. Then, the micrograph was overlaid with 100 nm meshes, which represent the moiré lattice rotated clockwise or counterclockwise. Most edges are parallel to the meshes, which supports the assumption. The lattice mismatch of the two crystalline phases produced round-square shaped islands on the wafer surface. The micrograph depicted in Figure 3b is shown in Figure S1 in the Supporting Information with blue colored bars to mark island edges parallel to the rotated meshes.

Regularly separated step-like structures provided a common and characteristic feature on real photocatalyst particles of $NaTaO_3$ doped with Ca, Sr, Ba,[3−5] or La cations[1,2] and $KTaO_3$ doped with Sr cations.[11] The solid solutions of $NaTaO_3$ with $LaIrO_3$,[54] $LaCrO_3$,[33] and $LaFeO_3$[37] prepared for visible-light harvesting also exhibited surface restructuring with 10 nm-long steps. These steps were proposed to spontaneously appear to correct the lattice mismatch at the core–shell interfaces.[52] The island formation driven by the crystalline moiré, which was observed in this study, mimics the nanometer-scale restructuring that occurs on the real photocatalyst particles.

3.3. Local Structure Around Ta and Ca Cations. The long-range ordered structure of the doped wafer was characterized with X-ray diffraction to indicate lattice contraction by 4%, as described in 3.1. In this subsection, the local structures around Ta and Ca cations are determined by using X-ray fluorescence holography. This is a model-free method for determining the three-dimensional (3D) structure of the local atomic arrangements around a specific fluorescing element.[55] A crystalline wafer is irradiated with a plane-wave X-ray of wavelength λ (Figure 4). Atom B that is adjacent to the fluorescing atom A scatters the incident X-ray. The scattered wave superimposed on the incident wave creates a standing wave to excite atom A. The fluorescent X-ray intensity $I(\theta)$ is proportional to the standing wave intensity on atom A and is expressed as follows

https://dx.doi.org/10.1021/acs.chemmater.9b04094
Chem. Mater. 2020, 32, 1439−1447

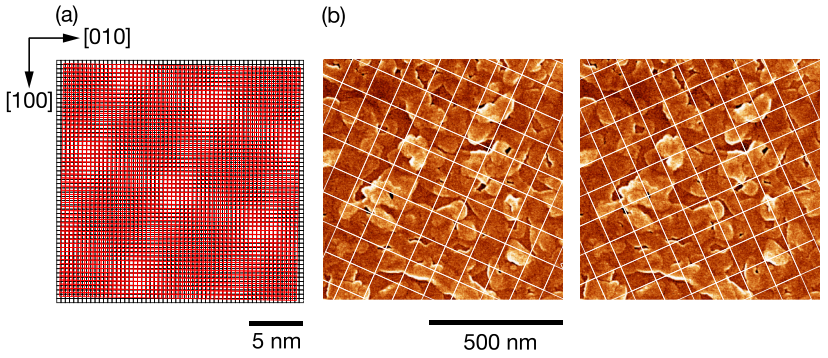

Figure 3. Mismatched lattices on the $KTaO_3$ (001) wafer doped with Ca cations. (a) $KTaO_3$ substrate and the Ca-containing surface layer are presented as black and red meshes, respectively. The red mesh length is contracted by 4% relative to the black mesh length, and the red meshes are rotated clockwise by 1° relative to the black meshes. (b) Scanning electron micrograph of the doped wafer was overlaid with 100 nm meshes rotated clockwise or counterclockwise by 24°.

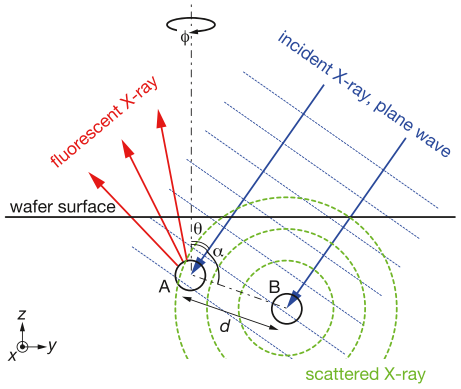

Figure 4. X-ray fluorescence induced by the X-ray standing wave.

$$I(\theta) = 1 - 2\mathrm{Re}\left(\frac{\lambda r_e f(\alpha)}{2\pi d} e^{2\pi i d(\cos\alpha - 1)/\lambda}\right)$$

with the X-ray scattering factor of the atom B $f(\alpha)$, A-to-B distance d, and electron radius r_e. The second term is sensitive to the local structure around the fluorescing atom and creates a hologram, while its amplitude is on the order of 10^{-3} relative to the first term, which produces background. The 3D distribution of X-ray scattering atoms is reconstructed around the fluorescing atom A by the application of Barton's algorithm[51] to holograms that were determined with incident X-ray of different wavelengths.

By tuning the X-ray energy for excitation and detection, one particular element is selectively characterized in an object that includes multiple elements. The feasibility of element-specific characterization of materials has been demonstrated in superconductors,[56] alloys,[57−59] and topological insulators.[60] The local structure around metal cations in perovskite-structured metal oxides, $SrTiO_3$[61] and $Pb(Mg_{1/3}Nb_{2/3})O_3$,[62] were analyzed. The application to guest-element atoms in a host lattice was examined in a numerical simulation of magnetic ions in wurtzite GaN.[63] The application to photocatalyst materials is experimentally examined in this study.

When guest cations are located in a host lattice to present a long-range order, X-ray diffraction provides an efficient method for determining their local structure. However, the long-range order of guest cations is often lost, as was the case in the doped wafer examined in this study. In the absence of the long-range order, the diffraction-based methods provide only the size and orientation of unit cells as was conducted in 3.1. By analyzing X-ray absorption fine structure, the distance from a guest cation to host atoms is given with the corresponding coordination number, even in the absence of long-range order. X-ray fluorescence holography further provides three-dimensional coordinates of the guest cation relative to host atoms. Two occupation sites accidentally possessing similar guest-to-host atom distances can be separated in X-ray fluorescence holography, not in X-ray absorption fine structure.

3.3.1. Tantalum Lα Holograms. During the measurement of the $KTaO_3$ wafer doped with Ca cations, $I(\theta)$ was observed using a solid-state detector in a θ range of 0−75° in 1° steps at one azimuth angle, ϕ. Similar θ scans were repeated at different ϕ values of 0−360° in steps of 0.25° to complete one hologram, $I(\theta,\phi)$. A typical acquisition time with Ta Lα fluorescence was 1 h per hologram. Eight holograms were acquired in the incident X-ray energy range of 10.0−13.5 keV with 0.5 keV steps. The background was subtracted from the raw $I(\theta,\phi)$ according to a previous study.[64] A hologram observed with an incident X-ray of 10.0 keV is shown in Figure 5a.

The 3D distribution of X-ray scattering atoms was reconstructed in a cubic volume of $(0.9\ \mathrm{nm})^3$ centered at the fluorescing Ta cation, where x-, y-, and z-axes are parallel to the [100], [010], and [001] directions of the $KTaO_3$ lattice, respectively. The positions of reconstructed atoms were consistent with that of the Ta cation sublattice in $KTaO_3$. Two-dimensional slices were extracted from the volume to quantitatively examine the reconstructed atom distribution. The fluorescing Ta cation is placed at the center of the slice at $z = 0$, as shown in Figure 5b. Four first-nearest Ta cations appeared at (±0.40 nm, 0) and (0, ±0.40 nm), as predicted for the $KTaO_3$ lattice. Four second-nearest Ta cations were at (±0.40, ±0.40 nm). Together with third-, fourth-, and fifth-nearest Ta cations, square meshes with a unit cell length of 0.40 nm were recognized on the Ta cation sublattice. The other reconstructed objects with weak scattering intensity were ascribed to artifacts produced during the numerical process of reconstruction.

Oxygen anions located on the $z = 0$ plane were missing. The first-nearest anions are present at (0.20 nm, 0) and equivalent positions, if they were recognized. The limited X-ray scattering power of oxygen is the reason for the missing anions. The reconstructed scattering intensity should be proportional to the X-ray scattering factor and to the atomic number of the

https://dx.doi.org/10.1021/acs.chemmater.9b04094
Chem. Mater. 2020, 32, 1439−1447

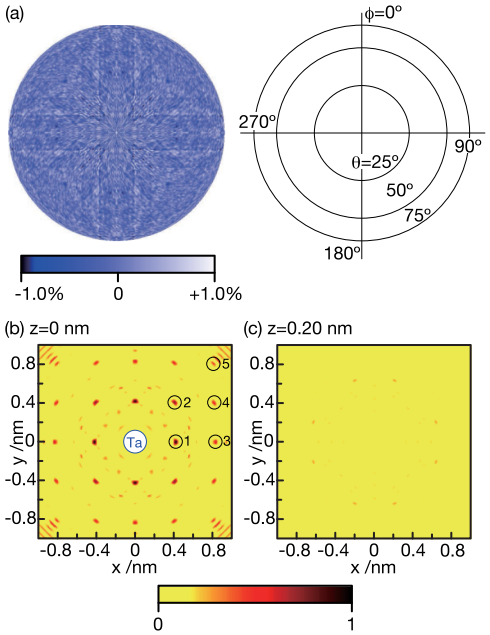

Figure 5. Ta Lα fluorescence holography applied to the $KTaO_3$ wafer doped with Ca. (a) Orthographic projection of the hologram with an incident X-ray energy of 10.0 keV. Intense and weak fluorescence are shown as bright and dark blue colors. The scale bar shows hologram intensity relative to the background intensity. The (θ, ϕ) coordinate in the orthographic projection is illustrated. The spatial distribution of X-ray scattering atoms reconstructed with eight holograms are presented on a plane of z = (b) 0 and (c) 0.2 nm. Intense and weak scattering are represented by a red-to-yellow color scale. The scale bar at the bottom shows scattering intensity normalized to 0−1. The fluorescing Ta cation is located at (0, 0, 0) and is labeled as "Ta". Each first-, second-, third-, fourth-, and fifth-nearest Ta cation is marked with numbered circles in (b).

scattering cation or anion. This relation allows for the assumption of the dominant role of Ta cations over O anions. The contribution of first-nearest K cations was also missing on the slice at z = 0.20 nm shown in Figure 5c; these cations would be present at (±0.20, ±0.20 nm). The missing K cations supported the assumption of the dominant X-ray scattering by Ta cations in $KTaO_3$. The holograms obtained with Ca fluorescence X-ray will be interpreted based on this assumption. Weak scattering at (0.60, 0.20 nm) and equivalent positions in Figure 5c were attributed to artifacts.

The two phases detected in X-ray diffraction should contribute to the holograms and thereby to the reconstructed atom distribution. However, the lattice contraction by 4% and rotation by ±1° relative to the substrate was not sufficient to be recognized in the reconstructed distributions.

3.3.2. Calcium Kβ Holograms. The holograms of calcium fluorescence were recorded and analyzed in a similar manner. Unfortunately, the most intense K$\alpha_{1,2}$ fluorescence of calcium at 3692−3688 eV overlapped with the Kβ fluorescence of potassium at 3590 eV. The energy resolution of the solid-state detector was not sufficient to separate calcium and potassium emissions. To avoid the undesired contribution of potassium fluorescence, the energy window of the detector was tuned to calcium Kβ fluorescence at 4013 eV. The limited yield of Ca Kβ fluorescence, 9% relative to that of Ca Kα fluorescence,[65] required a long acquisition time—typically 4 h per hologram. Eight holograms were acquired in an incident X-ray energy range of 6.0−9.5 keV with 0.5 keV steps. A background-subtracted hologram at 8.0 keV is shown in Figure 6a.

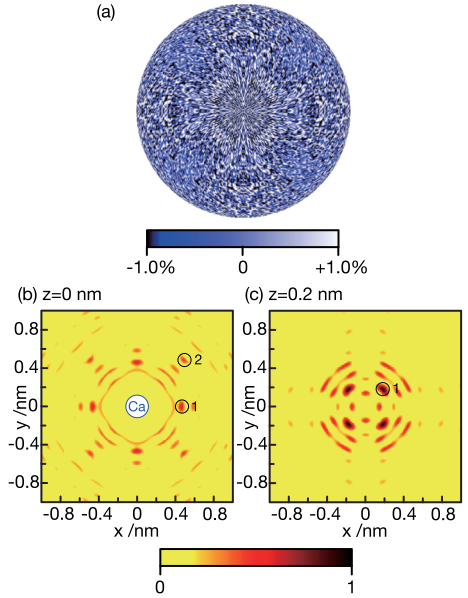

Figure 6. Ca Kβ fluorescence holography applied to the $KTaO_3$ wafer doped with Ca. (a) Orthographic projection of the hologram with an incident X-ray energy of 8.0 keV. The spatial distribution of X-ray scattering atoms reconstructed with the eight holograms are presented on a plane of z = (b) 0 and (c) 0.2 nm. The fluorescing Ca cation is located at (0, 0, 0) and labeled as "Ca". The first- and second-nearest Ta cations are marked with numbered circles in (b,c).

The spatial distribution of X-ray scattering atoms was reconstructed in a cubic volume with the fluorescing Ca cation placed at the cube center. The reconstructed distribution was partially similar to and partially different from the distribution deduced from the Ta Lα holograms. Two slices were extracted from the volume to examine the similar and different features.

In the slice at z = 0, four first-nearest atoms appeared on a square lattice at (0.46 nm, 0) and three equivalent positions, as shown in Figure 6b. Second-nearest atoms were recognized at (0.50, 0.50 nm) and at equivalent positions. We assigned these eight atoms to Ta cations according to our assumption that Ta cations dominate X-ray scattering in $KTaO_3$. The third-, fourth-, and fifth-nearest cations, which appeared in Figure 5b, are missing in Figure 6b. The missing cations suggest less ordered atom positions around the Ca cation than those around the Ta cation in the same wafer.

The Ta cation sublattice is cubic, with a side length of 0.40 nm in pristine $KTaO_3$. Notably, the square lattice with this side length was recognized in the atom positions reconstructed around the fluorescing Ta cation (Figure 5b). The eight atoms reconstructed in Figure 6b were located along the identical symmetry with small outward displacements. The identical symmetry allowed us to claim that the fluorescing Ca cation was embedded in the $KTaO_3$ lattice by settling at the position originally occupied by a Ta cation.

The first-nearest Ta cations shifted outward, away from the fluorescing Ca cation, by 0.06 nm compared with those reconstructed around the fluorescing Ta cation. The second-nearest Ta cations shifted away by 0.14 nm relative to those around the fluorescing Ta cation. Doping with Ca cations induced a local expansion of the B-site cation sublattice. The

https://dx.doi.org/10.1021/acs.chemmater.9b04094
Chem. Mater. 2020, 32, 1439−1447

outward displacement of the first-nearest cations was as large as 15% relative to the unperturbed Ta−Ta distance, 0.399 nm. The cation radii of six-fold coordinated Ca^{2+} and Ta^{5+} are defined to be 0.100 and 0.064 nm, respectively.[66] The difference in the radii of 0.034 nm may be the reason for the local expansion of the B-site cation sublattice.

The slice at z = 0.2 nm in Figure 6c showed a feature different from what was reconstructed from the Ta holograms (Figure 5c). Four atoms appeared at (±0.18, ±0.18 nm), which were absent in the atom distribution reconstructed around the fluorescing Ta cation. We assigned the four atoms to Ta cations on the basis of the X-ray scattering factor governed by atomic numbers. The fluorescing calcium cation, when settled in the B site of the $KTaO_3$ lattice, cannot be accompanied by Ta cations on the plane of z = 0.2 nm. When the fluorescing Ca cation occupies the A site by exchanging a potassium cation, four Ta cations at the neighboring B sites are present at (±0.20, ±0.20 nm) on the plane of z = 0.2 nm. Hence, the reconstructed distribution in Figure 6c indicates the Ca cation placed at the A site. An inward displacement by 0.03 nm relative to the theoretical position was additionally revealed.

The Ta cation distribution reconstructed on the plane at z = 0 indicated a fluorescing Ca cation settling in the B site. However, the distribution on the plane at z = 0.2 nm indicated a Ca cation placed at the A site. We can accept the two statements only when Ca cations exchanged A-site and B-site cations simultaneously. Calcium cations occupying A sites generated one hologram at one incident X-ray energy. Those at the B sites produced another hologram. The intensities of the two holograms were simply summed[67] and recorded by the detector. The atom distribution reconstructed from a set of the summed holograms presented the superposition of the atom distributions around the Ca cations at the A and B sites.

The site-sensitive occupation probability of Ca cations was further estimated. Let us assume a virtual compound, $CaTaO_3$, in which every potassium cation in $KTaO_3$ is replaced with a Ca cation. The balance of ionic charges and lattice deformation induced by cation replacement are ignored. A spherical particle of the virtual compound with a radius of 5 nm, which contained 41,309 atoms, was generated in silico. Eight Ca Kβ holograms of the particle were simulated with incident X-ray energies of 6.0−9.5 keV with 0.5 keV steps. The tantalum cation distribution was reconstructed using simulated holograms: this procedure is the same as the one used for the real holograms. The atom distribution reconstructed on the simulated holograms is available in Figure S2a. The first-nearest Ta cation to the Ca cation exhibited a scattering intensity 20 times larger in the reconstructed atom distribution of the virtual compound than that in the atom distribution shown in Figure 6c. Thus, the Ca occupation at the A site was estimated to be 5%.

A particle of virtual $KCaO_3$ was assumed, and eight Ca Kβ holograms were simulated in a similar manner. The atom distribution reconstructed on the simulated holograms is in Figure S2b. By comparing the scattering intensity in the virtual and real compounds, a Ca occupation of 6% at the B site was required. A composition of $(K_{0.95}Ca_{0.05})(Ta_{0.94}Ca_{0.06})O_{2.94}$ was expected by balancing the ionic charges with no cation vacancy. The occupation probability of the doping element was nearly even at the two cation sites. The Ca concentration estimated here was smaller than the composition of the wafer separately determined in 2.1, Ca/K/Ta = 22:30:48. In the second paragraph of this subsection, the authors suggested less ordered atom positions around the Ca cation than those around the Ta cation. The less ordered atom positions can decrease the scattering intensity in the reconstructed atom distribution. This decrease can be the reason for the Ca concentration underestimated in the reconstructed distribution. Thermal vibration in the real $KTaO_3$ should further decrease the intensity in the reconstructed atom distribution leading to underestimated Ca occupations. However, the extent of underestimation was not more than 7% with the Debye temperature of 449 K[68] of the pristine $KTaO_3$.

The simultaneous cation exchange hypothesized here is consistent with previous findings in real photocatalysts. In $NaTaO_3$[52] and $KTaO_3$[11] photocatalyst particles, Na or K cations at the A site and Ta cations at the B site were simultaneously doped with Ca, Sr, or Ba cations. In the present study, we are modeling the real photocatalyst particles with $KTaO_3$ wafers doped with Ca cations. As desired, the atom-scale structure of the photocatalysts and the simultaneous A- and B-site cation doping were successfully simulated in the wafers.

Finally, consider the possible origin of the lattice contraction by 4% determined by X-ray diffraction. The ionic radius of Ca cation is 0.134 nm when it is 12-fold coordinated.[66] When a Ca cation occupies the A site instead of a potassium cation, the 12-fold coordinated radius of which is 0.164 nm,[66] the perovskite-structured lattice should contract locally. Accordingly, an inward displacement of 0.03 nm was observed for the Ta cations first-nearest to the fluorescing Ca cation in Figure 6c. However, the Ca cation occupying the B site induced a local lattice expansion compared with the atom distribution on the plane of z = 0 in Figure 5b. The lattice size of the simultaneously exchanged compound is determined on the balance of the opposite contributions. The lattice contraction found in diffraction suggested a major role of Ca cations at the A site in reducing the lattice volume. This finding is consistent with the received picture of perovskite-structured compounds; the lattice volume is sensitive to the A-site cation radius.[69]

4. CONCLUSIONS

(001)-oriented $KTaO_3$ wafers were doped with Ca cations thorough the solid-state reaction to mimic $KTaO_3$ and $NaTaO_3$ photocatalysts. A wafer doped at a Ca/Ta molar ratio of 46% was characterized. X-ray diffraction showed a Ca-containing, perovskite-structured surface layer covering the substrate. The lattice of the surface layer was contracted by 4% and rotated by ±1° relative to the substrate lattice. The heteroepitaxial junction of the Ca-containing surface layer and the substrate simulated the core−shell structure found in real photocatalyst particles doped with alkaline earth metal cations. Round-square-shaped islands with 50−100 nm side lengths spontaneously appeared on the wafer surface to correct the lattice mismatch across the surface−substrate junction. The atom-scale structure around the Ta and Ca cations was determined with X-ray fluorescence holography. The first-, second-, third-, fourth-, and fifth-nearest Ta cations were recognized around the Ta cation emitting Lα fluorescence, whereas the neighboring K cations and O anions were not. The element-specific recognition allowed us to assume dominant X-ray scattering by Ta cations over the other light elements in $KTaO_3$. Holograms obtained with Ca Kβ fluorescence were analyzed based on this assumption to evidence a simultaneous exchange of A-site (K) and B-site (Ta) cations with Ca cations,

https://dx.doi.org/10.1021/acs.chemmater.9b04094
Chem. Mater. 2020, 32, 1439−1447

which was observed in real photocatalysts. Local lattice contraction and expansion were quantitatively determined around the Ca cations occupying the A and B sites, respectively.

The major features of the real photocatalysts—heteroepitaxial surface−bulk junctions, surface restructuring to correct mismatched lattices, and simultaneous cation exchange—were successfully reproduced in the wafer characterized in this study. $KTaO_3$ wafers that were doped in a similar manner should provide a promising class of photocatalyst models to study surface reaction centers for the water-splitting reaction. The ability of X-ray fluorescence holography to determine a local structure around doping cations in their host lattice was also demonstrated.

■ ASSOCIATED CONTENT

Supporting Information

The Supporting Information is available free of charge at https://pubs.acs.org/doi/10.1021/acs.chemmater.9b04094.

Marked scanning electron micrographs and atom distributions reconstructed from the simulated X-ray fluorescence holograms (PDF)

■ AUTHOR INFORMATION

Corresponding Author

Hiroshi Onishi − *Department of Chemistry, School of Science, Kobe University, Kobe 657-8501, Japan;* orcid.org/0000-0003-1873-9105; Email: oni@kobe-u.ac.jp

Authors

Tomoya Fujiwara − *Department of Chemistry, School of Science, Kobe University, Kobe 657-8501, Japan*

Akira Sasahara − *Department of Chemistry, School of Science, Kobe University, Kobe 657-8501, Japan*

Naohisa Happo − *Graduate School of Information Sciences, Hiroshima City University, Hiroshima 731-3194, Japan*

Koji Kimura − *Department of Physical Science and Engineering, Nagoya Institute of Technology, Nagoya 466-8555, Japan*

Kouichi Hayashi − *Department of Physical Science and Engineering and Frontier Research Institute for Materials Science, Nagoya Institute of Technology, Nagoya 466-8555, Japan*

Complete contact information is available at: https://pubs.acs.org/10.1021/acs.chemmater.9b04094

Author Contributions

The manuscript was written through contributions from all authors.

Notes

The authors declare no competing financial interest.

■ ACKNOWLEDGMENTS

Yoshihiro Ebisu and Takuya Ogura helped the authors with the observation of X-ray fluorescence holograms. Mitsunori Kitta prepared the graphics shown in TOC using VESTA software.[70] Hidenori Saito operated the scanning electron microscopy instrument. X-ray fluorescence holograms were observed on the BL13XU at SPring-8 with the approval of the Japan Synchrotron Radiation Research Institute (proposal nos. 2015B0116, 2016B1107, and 2017A1079). The financial support of JSPS KAKENHI grant numbers JP15H01046, JP16H02250, 16H03849, 18KK0161, and 26105006 are acknowledged.

■ REFERENCES

(1) Kudo, A.; Kato, H. Effect of Lanthanide-Doping into $NaTaO_3$ Photocatalysts for Efficient Water Splitting. *Chem. Phys. Lett.* **2000**, *331*, 373−377.

(2) Kato, H.; Asakura, K.; Kudo, A. Highly Efficient Water Splitting into H_2 and O_2 over Lanthanum-Doped $NaTaO_3$ Photocatalysts with High Crystallinity and Surface Nanostructure. *J. Am. Chem. Soc.* **2003**, *125*, 3082−3089.

(3) Iwase, A.; Kato, H.; Okutomi, H.; Kudo, A. Formation of Surface Nano-Step Structures and Improvement of Photocatalytic Activities of $NaTaO_3$ by Doping of Alkaline Earth Metal Ions. *Chem. Lett.* **2004**, *33*, 1260−1261.

(4) Maruyama, M.; Iwase, A.; Kato, H.; Kudo, A.; Onishi, H. Time-Resolved Infrared Absorption Study of $NaTaO_3$ Photocatalysts Doped with Alkali Earth Metals. *J. Phys. Chem. C* **2009**, *113*, 13918−13923.

(5) Iwase, A.; Kato, H.; Kudo, A. The Effect of Alkaline Earth Metal Ion Dopants on Photocatalytic Water Splitting by $NaTaO_3$ Powder. *ChemSusChem* **2009**, *2*, 783−787.

(6) Kato, H.; Kudo, A. New Tantalate Photocaralysts for Water Decomposition into H_2 and O_2. *Chem. Phys. Lett.* **1998**, *295*, 487−492.

(7) Mitsui, C.; Nishiguchi, H.; Fukamachi, K.; Ishihara, T.; Takita, Y. Photocatalytic Decomposition of Pure Water over NiO Supported on $KTa(M)O_3$ ($M=Ti^{4+}$, Hf^{4+}, Zr^{4+}) Perovskite Oxide. *Chem. Lett.* **1999**, 1327−1328.

(8) Ishihara, T.; Nishiguchi, H.; Fukamachi, K.; Takita, Y. Effects of Acceptor Doping to $KTaO_3$ on Photocatalytic Decomposition of Pure H_2O. *J. Phys. Chem. B* **1999**, *103*, 1−3.

(9) Kato, H.; Kudo, A. Water Splitting into H_2 and O_2 on Alkali Tantalate Photocatalysts $ATaO_3$ (A=Li, Na, and K). *J. Phys. Chem. B* **2001**, *105*, 4285−4292.

(10) Iwase, A.; Kato, H.; Kudo, A. Nanosized Au Particles as an Efficient Cocatalyst for Photocatalytic Overall Water Splitting. *Catal. Lett.* **2006**, *108*, 7−10.

(11) Sudrajat, H.; Dhakal, D.; Kitta, M.; Sasaki, T.; Ozawa, A.; Babel, S.; Yoshida, T.; Ichikuni, N.; Onishi, H. Electron Population and Water Splitting Activity Controlled by Strontium Cations Doped in $KTaO_3$ Photocatalysts. *J. Phys. Chem. C* **2019**, *123*, 18387−18397.

(12) Teramura, K.; Okuoka, S.-i.; Tsuneoka, H.; Shishido, T.; Tanaka, T. Photocatalytic Reduction of CO_2 Using H_2 as Reductant over $ATaO_3$ Photocatalysts (A = Li, Na, K). *Appl. Catal., B* **2010**, *96*, 565−568.

(13) Nakanishi, H.; Iizuka, K.; Takayama, T.; Iwase, A.; Kudo, A. Highly Active $NaTaO_3$-Based Photocatalysts for CO_2 Reduction to Form CO Using Water as the Electron Donor. *ChemSusChem* **2017**, *10*, 112−118.

(14) Li, K.; Handoko, A. D.; Khraisheh, M.; Tang, J. Photocatalytic Reduction of CO_2 and Protons Using Water as an Elecron Donor over Potassium Tantalate Nanoflakes. *Nanoscale* **2014**, *6*, 9767−9773.

(15) Shimura, K.; Kato, S.; Yoshida, T.; Itoh, H.; Hattori, T.; Yoshida, H. Photocatalytic Steam Reforming of Methane over Sodium Tantalate. *J. Phys. Chem. C* **2010**, *114*, 3493−3503.

(16) Yamamoto, A.; Mizuba, S.; Saeki, Y.; Yoshida, H. Platinum Loaded Sodium Tantalate Photocatalysts Prepared by a Flux Method for Photocatalytic Steam Reforming of Methane. *Appl. Catal., A* **2016**, *521*, 125−132.

(17) Fu, X.; Wang, X.; Leung, D. Y. C.; Xue, W.; Ding, Z.; Huang, H.; Fu, X. Photocatalytic Reforming of Glucose over La Doped Alkali Tantalate Photocatalysts for H_2 Production. *Catal. Commun.* **2010**, *12*, 184−187.

(18) Onishi, H. Sodium Tantalate Photocatalysts Doped with Metal Cations: Why Are They Active for Water Splitting? *ChemSusChem* **2019**, *12*, 1825−1834.

(19) Fujiwara, T.; An, L.; Park, Y.; Happo, N.; Hayashi, K.; Onishi, H. Heteroepitaxial Barium-Doped $NaTaO_3$ Films on $SrTiO_3(001)$ Substrate. *Thin Solid Films* **2018**, *658*, 66−72.
(20) Boddy, P. J.; Kahng, D.; Chen, Y. S. Oxygen Evolution on Potassium Tantalate Anodes. *Electrochim. Acta* **1968**, *13*, 1311−1328.
(21) Paulauskas, I. E.; Katz, J. E.; Jellison, G. E., Jr.; Lewis, L. A.; Brown, G. M.; Brown, G. M. Growth, Characterization, and Electrochemical Properties of Doped n-type $KTaO_3$ Photoanodes. *J. Electrochem. Soc.* **2009**, *156*, B580−B587.
(22) Ellis, A. B.; Kaiser, S. W.; Wrighton, M. S. Semiconducor Potassium Tantalate Electrodes. Photoassistance Agents for the Efficient Electrolysis of Water. *J. Phys. Chem.* **1976**, *80*, 1325−1328.
(23) Vousden, P. Study of the Unit-Cell Dimensions and Symmetry of Certain Ferroelectric Compounds of Niobium and Tantalum at Room Temperature. *Acta Crystallogr.* **1951**, *4*, 373−376.
(24) Kennedy, B. J.; Prodjosantoso, A. K.; Howard, C. J. Powder Neutron Diffraction Study of the High Temperature Phase Transitions in $NaTaO_3$. *J. Phys.: Condens. Matter* **1999**, *11*, 6319−6327.
(25) Kawasaki, S.; Nakatsuji, K.; Yoshinobu, J.; Komori, F.; Takahashi, R.; Lippmaa, M.; Mase, K.; Kudo, A. Epitaxial Rh-doped $SrTiO_3$ Thin Film Photocathode for Water Splitting under Visible Light Irradiation. *Appl. Phys. Lett.* **2012**, *101*, 033910.
(26) Kawasaki, S.; Takahashi, R.; Akagi, K.; Yoshinobu, J.; Komori, F.; Horiba, K.; Kumigashira, H.; Iwashina, K.; Kudo, A.; Lippmaa, M. Electronic Structure and Photoelectrochemical Properties of an Ir-Doped $SrTiO_3$ Photocatalyst. *J. Phys. Chem. C* **2014**, *118*, 20222−20228.
(27) Kawasaki, S.; Takahashi, R.; Lippmaa, M. Gradient Carrier Doping as a Method for Maximizing the Photon-to-Current Efficiency of a $SrTiO_3$ Water-Splitting Photoanode. *J. Phys. Chem. C* **2019**, *123*, 15551−15556.
(28) Bechstein, R.; Kitta, M.; Schütte, J.; Kühnle, A.; Onishi, H. Evidence for Vacancy Creation by Chromium Doping of $TiO_2(110)$. *J. Phys. Chem. C* **2009**, *113*, 3277−3280.
(29) Bechstein, R.; Kitta, M.; Schütte, J.; Onishi, H.; Kühnle, A. Effects of Antimony-Doping on the Surface Structure of Rutile $TiO_2(110)$. *Nanotechnology* **2009**, *20*, 264003.
(30) Bechstein, R.; Kitta, M.; Schütte, J.; Kühnle, A.; Onishi, H. Surface Reconstruction Induced by Transition Metal Doping of $TiO_2(110)$. *J. Phys. Chem. C* **2009**, *113*, 13199−13203.
(31) Kato, H.; Kudo, A. Water Splitting into H_2 and O_2 on Alkali Tantalate Photocatalysts $ATaO_3$ (A = Li, Na, and K). *J. Phys. Chem. B* **2001**, *105*, 4285−4292.
(32) Kanhere, P.; Shenai, P.; Chakraborty, S.; Ahuja, R.; Zheng, J.; Chen, Z. Mono-and co-doped $NaTaO_3$ for visible light photocatalysis. *Phys. Chem. Chem. Phys.* **2014**, *16*, 16085−16094.
(33) Yi, Z. G.; Ye, J. H. Band gap tuning of $Na_{1-x}La_xTa_{1-x}Cr_xO_3$ for H_2 generation from water under visible light irradiation. *J. Appl. Phys.* **2009**, *106*, 074910.
(34) Yang, M.; Huang, X.; Yan, S.; Li, Z.; Yu, T.; Zou, Z. Improved hydrogen evolution activities under visible light irradiation over $NaTaO_3$ codoped with lanthanum and chromium. *Mater. Chem. Phys.* **2010**, *121*, 506−510.
(35) Kang, H. W.; Lim, S. N.; Park, S. B.; Park, A.-H. A. H_2 evolution under visible light irradiation on La and Cr co-doped $NaTaO_3$ prepared by spray pyrolysis from polymeric precursor. *Int. J. Hydrogen Energy* **2013**, *38*, 6323−6334.
(36) Sudrajat, H.; Zhou, Y.; Sasaki, T.; Ichikuni, N.; Onishi, H. The atomic-scale structure of $LaCrO_3$−$NaTaO_3$ solid solution photocatalysts with enhanced electron population. *Phys. Chem. Chem. Phys.* **2019**, *21*, 5148−5157.
(37) Kanhere, P.; Nisar, J.; Tang, Y.; Pathak, B.; Ahuja, R.; Zheng, J.; Chen, Z. Electronic structure, optical properties, and photocatalytic activities of $LaFeO_3$−$NaTaO_3$ solid solution. *J. Phys. Chem. C* **2012**, *116*, 22767−22773.
(38) Sudrajat, H.; Ichikuni, N.; Onishi, H. Visible Light Responsive La and Fe Co-Doped $NaTaO_3$ Photocatalysts: Local Structure around Dopants. *Chem. Phys.* **2020**, *531*, 110648.
(39) Yi, Z. G.; Ye, J. H. Band gap tuning of $Na_{1-x}La_xTa_{1-x}Co_xO_3$ solid solutions for visible light photocatalysis. *Appl. Phys. Lett.* **2007**, *91*, 254108.
(40) Sudrajat, H.; Kitta, M.; Ichikuni, N.; Onishi, H. Double Doping of $NaTaO_3$ Photocatalysts with La and Mn for Strongly Enhanced Visible-Light Absorption. *ACS Appl. Energy Mater.* **2019**, *2*, 7518−7526.
(41) Kim, Y.-I.; Woodward, P. M.; Baba-Kishi, K. Z.; Tai, C. W. Characterization of the Structural, Optical, and Dielectric Properties of Oxynitride Perovskites AMO_2N (A = Ba, Sr, Ca; M = Ta, Nb). *Chem. Mater.* **2004**, *16*, 1267−1276.
(42) Zhao, Z.; Li, R.; Li, Z.; Zou, Z. Photocatalytic activity of La−N-codoped $NaTaO_3$ for H_2 evolution from water under visible-light irradiation. *J. Phys. D: Appl. Phys.* **2011**, *44*, 165401.
(43) Balaz, S.; Porter, S. H.; Woodward, P. M.; Brillson, L. J. Electric Structure of Tantalum Oxynitride Perovskite Photocatalysts. *Chem. Mater.* **2013**, *25*, 3337−3343.
(44) Ueda, K.; Kato, H.; Kobayashi, M.; Hara, M.; Kakihana, M. Control of valence band potential and photocatalytic properties of $Na_xLa_{1-x}TaO_{1+2x}N_{2-2x}$ oxynitride solid solutions. *J. Mater. Chem. A* **2013**, *1*, 3667−3674.
(45) Pan, C.; Takata, T.; Nakabayashi, M.; Matsumoto, T.; Shibata, N.; Ikuhara, Y.; Domen, K. A Complex Perovskite-Type Oxynitride: The First Photocatalyst for Water Splitting Operable at up to 600 nm. *Angew. Chem., Int. Ed.* **2015**, *54*, 2955−2959.
(46) Oka, D.; Hirose, Y.; Kamisaka, H.; Fukumura, T.; Sasa, K.; Ishii, S.; Matsuzaki, H.; Sato, Y.; Ikuhara, Y.; Hasegawa, T. Possible ferroelectricity in perovskite oxynitride $SrTaO_2N$ epitaxial thin films. *Sci. Rep.* **2015**, *4*, 4987.
(47) Si, W.; Pergolesi, D.; Haydous, F.; Fluri, A.; Wokaun, A.; Lippert, T. Investigating the behavior of various cocatalysts on $LaTaON_2$ photoanode for visible light water splitting. *Phys. Chem. Chem. Phys.* **2017**, *19*, 656−662.
(48) An, L.; Sasaki, T.; Weidler, P. G.; Wöll, C.; Ichikuni, N.; Onishi, H. Local Environment of Strontium Cations Activating $NaTaO_3$ Photocatalysts. *ACS Catal.* **2018**, *8*, 880−885.
(49) Happo, N.; Hada, T.; Kubota, A.; Ebisu, Y.; Hosokawa, S.; Kimura, K.; Tajiri, H.; Matsushita, T.; Hayashi, K. Improvement of Graphite Crystal Analyzer for Light Elements on X-ray Fluorescence Holography Measurement. *Jpn. J. Appl. Phys.* **2018**, *57*, 058006.
(50) Matsushita, T.; Muro, T.; Matsui, F.; Happo, N.; Hosokawa, S.; Ohyama, K.; Sato-Tomita, A.; Sasaki, Y. C.; Hayashi, K. Principle and Reconstruction Algorithm for Atomic-Resolution Holography. *J. Phys. Soc. Jpn.* **2018**, *87*, 0601002.
(51) Barton, J. J. Removing Multiple Scattering and Twin Images from Holographic Images. *Phys. Rev. Lett.* **1991**, *67*, 3106−3109.
(52) An, L.; Onishi, H. Electron-Hole Recombination Controlled by Metal Doping Sites in $NaTaO_3$ Photocatalysts. *ACS Catal.* **2015**, *5*, 3196−3206.
(53) An, L.; Kitta, M.; Iwase, A.; Kudo, A.; Ichikuni, N.; Onishi, H. Photoexcited Electrons Driven by Doping Concentration Gradient: Flux-Prepared $NaTaO_3$ Photocatalysts Doped with Strontium Cations. *ACS Catal.* **2018**, *8*, 9334−9341.
(54) Iwase, A.; Saito, K.; Kudo, A. Sensitization of $NaMO_3$ (M: Nb and Ta) Photocatalysts with Wide Band Gap to Visible Light by Ir doping. *Bull. Chem. Soc. Jpn.* **2009**, *82*, 514−518.
(55) Hayashi, K.; Korecki, P. X-Ray Fluorescence Holography: Principles, Apparatus, and Applications. *J. Phys. Soc. Jpn.* **2018**, *87*, 061003.
(56) Kudo, K.; Ioka, S.; Happo, N.; Ota, H.; Ebisu, Y.; Kimura, K.; Hada, T.; Kimura, T.; Tajiri, H.; Hosokawa, S.; Hayashi, K.; Nohara, M. Impact of Local Atomic Fluctuations on Superconductivity of Pr-Substituted $CaFe_2As_2$ Studied by X-ray Fluorescence Holography. *J. Phys. Soc. Jpn.* **2019**, *88*, 063704.
(57) Marchesini, S.; Schmithüsen, F.; Tegze, M.; Faigel, G.; Calvayrac, Y.; Belakhovsky, M.; Chevrier, J.; Simionovici, A. S. Direct 3D Imaging of $Al_{70.4}Pd_{21}Mn_{8.6}$ Quasicrystal Local Atomic Structure by X-ray Holography. *Phys. Rev. Lett.* **2000**, *85*, 4723−4726.

https://dx.doi.org/10.1021/acs.chemmater.9b04094
Chem. Mater. 2020, 32, 1439−1447

(58) Nishioka, T.; Yamamoto, Y.; Kimura, K.; Hagihara, K.; Izuno, H.; Happo, N.; Hosokawa, S.; Abe, E.; Suzuki, M.; Matsushita, T.; Hayashi, K. In-Plane Positional Correlations among Dopants in 10H Type Long Period Stacking Ordered $Mg_{75}Zn_{10}Y_{15}$ Alloy Studied by X-ray Fluorescence Holography. *Materialia* **2018**, *3*, 256−259.
(59) Dąbrowski, K. M.; Dul, D. T.; Jaworska-Gołąb, T.; Rysz, J.; Korecki, P. X-ray fluorescence holography studies for a Cu_3Au crystal. *Nucl. Instrum. Methods Phys. Res., Sect. B* **2015**, *364*, 136−141.
(60) Hosokawa, S.; Stellhorn, J. R.; Matsushita, T.; Happo, N.; Kimura, K.; Hayashi, K.; Ebisu, Y.; Ozaki, T.; Ikemoto, H.; Setoyama, H.; Okajima, T.; Yoda, Y.; Ishii, H.; Liao, Y.-F.; Kitaura, M.; Sasaki, M. Impurity Position and Lattice Distortion in a Mn-Doped Bi_2Te_3 Topological Insulator Investigated by X-Ray fluorescence Holography and X-Ray Absorption Fine Structure. *Phys. Rev. B* **2017**, *96*, 214207.
(61) Tegze, M.; Faigel, G. X-ray holography with atomic resolution. *Nature* **1996**, *380*, 49−51.
(62) Hu, W.; Hayashi, K.; Ohwada, K.; Chen, J.; Happo, N.; Hosokawa, S.; Takahasi, M.; Bokov, A. A.; Ye, Z.-G. Acute and obtuse rhombohedrons in the local structures of relaxor ferroelectric $Pb(Mg_{1/3}Nb_{2/3})O_3$. *Phys. Rev. B: Condens. Matter Mater. Phys.* **2014**, *89*, 140103.
(63) Dul, D. T.; Korecki, P. Wavelet analysis of white beam x-ray fluorescence holograms: determination of lattice sites and imaging of local atomic structure. *New J. Phys.* **2012**, *14*, 113044.
(64) Happo, N.; Hayashi, K.; Hosokawa, S. Data Analysis of X-ray Fluorescence Holography by Subtracting Normal Component from Inverse Hologram. *Jpn. J. Appl. Phys.* **2010**, *49*, 116601.
(65) Thompson, A. C.; Attwood, D. T.; Gullikson, E. M.; Howells, M. R.; Kortright, J. B.; Robinson, A. L.; Underwood, J. H.; Kim, K.-J.; Kirz, J.; Lindau, I.; Pianetta, P.; Winick, H.; Williams, G. P.; Scofield, J. H. *X-ray Data Booklet*; Lawrence Berkeley National Laboratory, 2009. https://xdb.lbl.gov.
(66) Shannon, R. D. Revised Effective Ionic Radii and Systematic Studies of Interatomic Distances in Halides and Chalcogenides. *Acta Crystallogr., Sect. A: Cryst. Phys., Diffr., Theor. Gen. Crystallogr.* **1976**, *32*, 751−767.
(67) Here we assumed random exchange of the cations not to induce interference of fluorescent X-rays emitted by Ca cations occupying the A site and B site.
(68) Bourgeal, S.; Villar, R.; Vieira, S.; Trepakov, V. A. Low temperature specific heat of $KTaO_3$ from 0.3K. *Ferroelectrics* **1988**, *79*, 237−240.
(69) Tilley, R. J. D. *Perovskites: Structure−Property Relationships*; Wiley, 2016.
(70) Momma, K.; Izumi, F. VESTA3 for Three-Dimensional Visualization of Crystal, Volumetric and Morphology Data. *J. Appl. Crystallogr.* **2011**, *44*, 1272−1276.

https://dx.doi.org/10.1021/acs.chemmater.9b04094
Chem. Mater. 2020, 32, 1439−1447